Atmos. Meas. Tech. Discuss., 7, 6245–6285, 2014
www.atmos-meas-tech-discuss.net/7/6245/2014/
doi:10.5194/amtd-7-6245-2014

Atmospheric Measurement Techniques Discussions
Open Access

Measurements of diurnal variations and Eddy Covariance (EC) fluxes of glyoxal in the tropical marine boundary layer: description of the Fast LED-CE-DOAS instrument

S. Coburn[1,2], I. Ortega[1,2], R. Thalman[1,2,*], B. Blomquist[3], C. W. Fairall[4], and R. Volkamer[1,2]

[1]Department of Chemistry and Biochemistry, University of Colorado, Boulder, CO, USA
[2]CIRES – Cooperative Institute for Research in Environmental Sciences, Boulder, CO, USA
[3]Department of Oceanography, University of Hawaii, Honolulu, HI, USA
[4]Earth System Research Laboratory, NOAA, Boulder, CO, USA
[*]now at: Brookhaven National Laboratory, Upton, NY, USA

Received: 14 May 2014 – Accepted: 9 June 2014 – Published: 20 June 2014

Correspondence to: R. Volkamer (rainer.volkamer@colorado.edu)

Published by Copernicus Publications on behalf of the European Geosciences Union.

Abstract

Here we present first Eddy Covariance (EC) measurements of fluxes of glyoxal, the smallest α-dicarbonyl product of hydrocarbon oxidation, and a precursor for secondary organic aerosol (SOA). The unique physical and chemical properties of glyoxal, i.e., high solubility in water (Henry's Law constant, $K_H = 4.2 \times 10^5\,\mathrm{M\,atm^{-1}}$) and short atmospheric lifetime (~ 2 h at solar noon) make it a unique indicator species for organic carbon oxidation in the marine atmosphere. Previous reports of elevated glyoxal over oceans remain unexplained by atmospheric models. Here we describe a Fast Light Emitting Diode Cavity Enhanced Differential Optical Absorption Spectroscopy (Fast LED-CE-DOAS) instrument to measure diurnal variations and EC fluxes of glyoxal, and inform about its unknown sources. The fast in situ sensor is described, and first results are presented from a cruise deployment over the Eastern tropical Pacific Ocean (20° N to 10° S; 133° W to 85° W) as part of the Tropical Ocean Troposphere Exchange of Reactive Halogens and OVOC (TORERO) field experiment (January to March 2012). The Fast LED-CE-DOAS is a multispectral sensor that selectively and simultaneously measures glyoxal (CHOCHO), nitrogen dioxide (NO_2), oxygen dimers (O_4) and water vapor (H_2O) with ~ 2 Hz time resolution, and a precision of $\sim 40\,\mathrm{pptv\,Hz^{-0.5}}$ for glyoxal. The instrument is demonstrated to be a "white-noise" sensor suitable for EC flux measurements; further, highly sensitive and inherently calibrated glyoxal measurements are obtained from temporal averaging of data (~ 2 pptv detection limit over 1 h). The campaign averaged mixing ratio in the Southern Hemisphere (SH) is found to be 43 ± 9 pptv glyoxal, and is higher than in the Northern Hemisphere (NH: 32 ± 6 pptv; error reflects variability over multiple days). The diurnal variation of glyoxal in the MBL is measured for the first time, and mixing ratios vary by ~ 8 ppt (NH) and ~ 12 pptv (SH) over the course of 24 h. Consistently, maxima are observed at sunrise (NH: 35 ± 5 pptv; SH: 47 ± 7 pptv) and minima at dusk (NH: 27 ± 5 pptv; SH: 35 ± 8 pptv). Ours are the first EC flux measurements of glyoxal. In both hemispheres, the daytime flux was directed from the atmosphere into the ocean, indicating that the ocean is a net sink for glyoxal

AMTD
7, 6245–6285, 2014

during the day. After sunset the ocean was a source for glyoxal to the atmosphere (positive flux) in the SH; this primary ocean source was operative throughout the night. In the NH, the nighttime flux was positive only shortly after sunset, and negative during most of the night. Positive EC fluxes of soluble glyoxal over oceans indicate the presence of an ocean surface organic microlayer (SML), and locate a glyoxal source within the SML. The origin of atmospheric glyoxal, and possibly other oxygenated hydrocarbons over tropical oceans warrants further investigation.

1 Introduction

Eddy covariance (EC) fluxes are a well-established and widely used technique to measure surface-atmosphere gas exchange. The EC flux method provides insight into sources and sinks of atmospheric parameters (physical, chemical state variables) suitable to test our process level understanding (Baldocchi et al., 2001). EC fluxes are defined as the time average covariance between deviations from the mean of vertical wind velocity and deviations from the mean in the parameter of interest, e.g. here, the mixing ratio of a trace gas:

$$F_c = \overline{w'c'} = \int_0^{f_n} C_{wc}(f)\mathrm{d}f \tag{1}$$

where F is the flux, w' is the vertical wind velocity component, c' is the mixing ratio of the trace gas component, the prime denotes the instantaneous deviation from the mean, f_n is the Nyquist frequency of the measurements, and C_{wc} is the cospectrum.

A requirement of the EC flux technique is that measurements of both vertical wind velocities and the trace gas of interest are performed at high sampling frequencies, f, (typically a minimum of several Hz), sufficient to capture a majority of those frequencies that contribute to the overall flux. Balancing this requirement with preserving sufficient

AMTD
7, 6245–6285, 2014

sensitivity in the measurements is one of the major challenges with developing chemical sensors suitable for EC flux applications. For mobile deployments, a portable and robust sensor is needed. Further, additional measurements of platform motion need to be performed, and corrections on the wind velocity data are needed. A description of the system deployed in this study and the method of correction is described by Fairall et al. (1997) and Edson et al. (1998), respectively. A particular challenge arises for EC flux measurements of short-lived species in the marine boundary layer (MBL), for which concentrations often do not exceed 10s to 100s of parts per trillion (1 pptv = 10^{-12} volume mixing ratio (VMR) = 2.46×10^{7} molec cm^{-3} at 298 K temperature and 1013 mbar pressure). As a result of these challenges, ship based EC flux measurements have today only been reported for the seven trace molecules: dimethyl sulfide (DMS) (Huebert et al., 2004; Blomquist et al., 2006, 2010; Marandino et al., 2007, 2008, 2009; Miller et al., 2009; Edson et al., 2011; Bell et al., 2013), Carbon dioxide (CO_2) (Fairall et al., 2000; McGillis et al., 2001, 2004; Kondo and Tsukamoto 2007; Miller et al., 2009, 2010; Taddei et al., 2009; Norman et al., 2012), Ozone (O_3) (Bariteau et al., 2010; Helmig et al., 2012), carbon monoxide (CO) (Blomquist et al., 2012), acetone (Marandino et al., 2005; Taddei et al., 2009; Yang et al., 2014), acetaldehyde (Yang et al., 2014), and methanol (Yang et al., 2013). Table 1 lists typical concentrations for these molecules in the MBL, and compares them with glyoxal in terms of their Henry's Law constants (K_H, at 298 K), and typical atmospheric lifetimes. Notably, glyoxal is the molecule with the shortest atmospheric lifetime, and is present in the lowest abundance. The short lifetime of glyoxal limits the spatial scale over which it can be transported in the atmosphere to few 10 km. Further, glyoxal is the most soluble molecule in Table 1, i.e. its Henry's Law constant is 2000, 13 860, and 30 000 times larger than that of the other oxygenated hydrocarbons (OVOC) methanol, acetone and acetaldehyde, respectively. The differences in the physical and chemical properties have fundamental implications for the air-sea exchange of glyoxal. For example, while it is possible to supersaturate the surface ocean with acetaldehyde (Zhou and Mopper, 1990; Kieber et al., 1990; Millet et al., 2010; Yang et al., 2014) it is impossible

AMTD
7, 6245–6285, 2014

to supersaturate the ocean with glyoxal (Sinreich et al., 2010). Studies measuring the waterside concentration of glyoxal have values in the nanomolar (nM) range (Zhou and Mopper, 1990: 0.5–5 nM; van Pinxteren and Herrmann, 2013: ~4 nM), while based on $K_{H,glyoxal}$ and an airside VMR of 50 pptv the expected seawater concentration should be ~20 000 nM. The low glyoxal abundance in the MBL and unique properties make glyoxal a particularly interesting, yet challenging molecule to measure EC fluxes. To the best of our knowledge there are no previous attempts to measure EC fluxes of glyoxal.

Glyoxal, the smallest α-dicarbonyl, is largely produced from the oxidation of Volatile Organic Compounds (VOCs) of both natural and anthropogenic origins (Myriokefalitakis et al., 2008; Stavrakou et al., 2009). It can also be directly emitted from sources such as biomass burning, fossil and biofuel combustion (Grosjean et al., 2001; Kean et al., 2001; Hays et al., 2002). Atmospheric removal of glyoxal is driven by photolysis, reaction with hydroxyl (OH) radicals, dry and wet deposition, and uptake to aerosols (Stavrakou et al., 2009). Additionally, glyoxal has been identified as an important Secondary Organic Aerosol (SOA) precursor (Liggio et al., 2005; Volkamer et al., 2007; Fu et al., 2008; Ervens and Volkamer, 2010; Waxman et al., 2013). There are currently only few reports of glyoxal measurements over oceans (Zhou and Mopper 1990; Sinreich et al., 2010; Mahajan et al., 2014). These data show significant variability in the abundance of glyoxal (25–140 pptv), and confirm the widespread presence of glyoxal over oceans that had been suggested by satellites (Wittrock et al., 2006; Lerot et al., 2010). Satellites find vertical column densities (VCDs) of 2–4 × 10^{14} molec cm^{-2} over the Eastern Pacific ocean, comparable to and exceeding the upper range of glyoxal mixing ratios observed in the MBL (assuming all glyoxal was located inside a 1 km high MBL). In situ observations hold great potential to inform this apparent mismatch, but there are no previous in situ measurements of glyoxal reported over oceans. While virtually all measurements of glyoxal have been made over land (Vrekoussis et al., 2009), our understanding of the sources, sinks, and chemical processing of this molecule in continental air masses remains poor. Known continental sources only account for ~50 % of the glyoxal budget based on VCDs from the SCanning Imaging Absorption spectroMeter

AMTD
7, 6245–6285, 2014

for Atmospheric CHartographY (SCIAMACHY) satellite (Stavrakou et al., 2009). Over the tropical ocean, atmospheric models predict virtually no glyoxal (Myriokefalitakis et al., 2008; Fu et al., 2008; Stavrakou et al., 2009); the presence of this molecule in the remote MBL, thousands of kilometers from continental sources, is surprising and currently not understood (Sinreich et al., 2010).

The University of Colorado Fast Light Emitting Diode Cavity Enhanced Differential Optical Absorption Spectroscopy (Fast-LED-CE-DOAS) instrument was developed to obtain new insights about the sources of glyoxal in the remote MBL. The following sections describe the instrument, characterize performance, and report first results from a ship deployment over the tropical Eastern Pacific Ocean during the TORERO field experiment.

2 Experimental

The TORERO 2012 field campaign was an extensive effort to measure a variety of atmospheric parameters and trace gases over the Eastern Tropical Pacific Ocean from aircraft and ships. The ship-based portion of the campaign took place aboard the NOAA RV *Ka'imimoana* on a research cruise leaving from Honolulu, HI to Puntarenas, Costa Rica between 25 January–1 March 2012 (37 days at sea). Figure 1 shows a map with the ship track. Also shown are HYSPLIT 5 day back trajectories for noon and midnight (local time) along the ship track for each day.

2.1 Fast LED-CE-DOAS instrument

Differential Optical Absorption Spectroscopy (DOAS) is a well-established technique that has been successfully used to measure a wide variety of atmospheric trace gases, including glyoxal (Platt, 1994). While traditionally DOAS measurements were conducted in the open atmosphere (Platt et al., 1979), the advent of CEAS measurements coupled with DOAS retrievals provides particularly sensitive measurements

AMTD
7, 6245–6285, 2014

(Thalman and Volkamer, 2010; Ryerson et al., 2013). The multispectral nature of the light sources, such as light emitting diodes (LEDs), add selectivity to enable the simultaneous detection of multiple trace gases, while preserving excellent sensitivity found in other in situ cavity enhanced techniques (e.g., cavity ring down spectroscopy) (Thalman and Volkamer, 2010; Ryerson et al., 2013). The Fast-LED-CE-DOAS instrument is a further development of the instrument described in Thalman and Volkamer (2010). In brief, an LED light source is coupled to an optical cavity enclosed by two highly reflective mirrors, which allows light paths inside the cavity to be realized that are much longer ($\sim 2 \times 10^4$ times) than the length of the cavity itself. The light is collected from the backside of the mirror opposite the LED by an optical fiber and directed onto the spectrometer slit (see Fig. 3).

For this system, a high-power LED (LedEngin) with peak emission near 465 nm was used in conjunction with custom coated mirrors (Advanced Thin Films) with peak reflectivity between 440–470 nm. The cavity had a base length of 86 cm (74.45 cm sample path length) and was coupled to a Princeton Instruments Acton SP2156 Czerny-Turner Imaging Spectrometer with a PIXIS 400B CCD detector (1340×400 pixels or 26.8×8 mm). The spectrometer utilized a custom 1000 g mm^{-1} grating blazed at 250 nm which covered the wavelength range from 390–530 nm with ~ 0.75 nm resolution (FWHM). The wavelength range observed simultaneously by our system was from 430 to 480 nm and allowed for the selective detection of glyoxal, NO_2, H_2O, and O_4. Two spectral fitting windows were utilized during this study; one optimized for the retrieval of glyoxal and the other for O_4. The glyoxal fitting window covered the wavelength range from 433–460 nm, the O_4 window covered the range 457–487 nm, and trace gas reference cross sections for glyoxal (Volkamer et al., 2005), H_2O (measured with this instrument), O_4 (Thalman and Volkamer, 2013), and NO_2 (Vandaele et al., 1998) were simultaneously fitted in both windows. Figure 2 shows spectral fit results from the DOAS analysis of these trace gases: the left column shows fits from the glyoxal analysis window for a clean period (no NO_2 contamination from the ship stack) and the right column shows spectral fits from the O_4 window where some NO_2 contamination

AMTD
7, 6245–6285, 2014

is present. The water measurement was used to monitor ambient conditions, NO_2 was used as a tracer for sampling the ship stack plume, and the O_4 measurement was used to correct the DOAS data for sampling time lag and inlet characterization (discussed in Sects. 3.1.1 and 3.1.2).

The primary measurement of the DOAS technique is Slant Column Density (SCD) which is the integrated concentration of the measured species along all light paths. It is easily converted using Lambert–Beer's Law to concentration if the light path length within the cavity is known. Two different methods were utilized to experimentally determine the cavity light path: (1) comparison of measured O_4 SCDs and the calculated concentration of O_4 within the cavity; and (2) using the ratio of the signal measured in two different pure gases whose Rayleigh scattering cross-sections are well known (Thalman and Volkamer, 2010). For this study, method 2 was employed and N_2 and He were used for this process (referred to as mirror curves from this point forward). Mirror curves were taken on a near daily basis which enabled the continuous monitoring of the cavity performance. Additionally, an inherent consistency check exists from the comparison of O_4 SCD measurements with those calculated from the mirror curve, the Rayleigh scattering cross section of air, and known temperature and pressure (Thalman and Volkamer, 2010). For the duration of the cruise, the peak mirror reflectivity was maintained between 99.9967–99.9973 %, translating into routine cavity path lengths of 18–20 km at 455 nm.

In order to accelerate the data acquisition of the instrument to rates sufficient to accommodate EC fluxes, software was developed to simultaneously eliminate shutter movements and decrease readout time (through binning of CCD rows). The final instrument measurement frequency of ~ 2 Hz strikes a balance between time resolution, and the duty cycle dedicated to collecting photons (as compared to read-out time of the CCD). The measurement detection limit with CE-DOAS measurements is typically photon shot-noise limited. We assess the instrument performance by investigating the root mean square (RMS) of the optical density of the residual remaining after the non-linear least squares fitting routine, and comparing it with the theoretical photon shot

AMTD
7, 6245–6285, 2014

noise (Coburn et al., 2011). Individual spectra were summed, and analyzed to improve the signal to noise ratio of the measurements. In an ideal instrument (i.e., completely limited by photo shot noise), the RMS of the fitting routine should follow photon counting statistics, where the theoretical RMS is inversely proportional to the square root of the number of photons collected.

$$\mathrm{RMS} \equiv \frac{1}{\sqrt{N}} \tag{2}$$

where N is the number of photons collected.

The measured RMS of the Fast LED-CE-DOAS instrument field deployment is compared to the theoretical RMS, and plotted as a function of the number of photons in Fig. 3. The grey points are raw data at different levels of averaging and the colored squares represent the median values for each set: light blue is the raw 400 ms data; dark blue is the sum of 5 spectra (~ 2 s); purple is the sum of 20 spectra (~ 8 s); red is the sum of 100 spectra (~ 40 s); and the green is the sum of 1000 spectra (~ 8 min). As can be seen, the RMS during this campaign fairly closely follows counting statistics for the measured spectra, as well as for different levels of binning. Shown on the right axis is the corresponding 1σ precision for glyoxal.

Appropriate quality assurance filters were applied to the raw CE-DOAS measurements prior to calculating glyoxal fluxes in order to exclude the use of any stack contamination, or otherwise questionable data. These filters removed periods of elevated NO_2 (contaminated by the ship stack plume: values greater than ~ 30 pptv), instability in the cavity (O_4 and internal cavity pressure measurements: acceptable pressure range 470–500 torr), and any spectra where the DOAS fitting resulted in RMS values larger than 5×10^{-3}.

2.2 TORERO field campaign

While the cruise started on 25 January 2012, only data taken 2–28 February 2012 will be considered for this study. The inlet for the cavity was mounted near the top of a 10 m

AMTD
7, 6245–6285, 2014

jackstaff (18 m a.s.l.) on the bow along with the inlets for the CO_2 flux system (Blomquist et al., 2014) and the in situ O_3 monitor, the sonic anemometer, and a motion system. The sampling line between the inlet and the instrument was ~ 65 m long, and consisted of 3/8″ ID coated aluminum tubing (Eaton SynFlex Type 1300). Additionally, an aerosol filter (changed every other day) was included after the inlet in order to prevent collection of sea salt in the sampling line, and keep the air reaching the CE-DOAS system aerosol free. The filter was regularly changed to avoid aerosol accumulation, and experiments of glyoxal transfer through Teflon filters showed no visible attenuation (Thalman and Volkamer, 2010). Previous experiments to characterize the effect of In order to maintain turbulent flow throughout the sampling line, a high flow pump maintained a flow of ~ 120 L min^{-1} (Lenschow and Raupach, 1991). From this main flow, a sample flow of ~ 9 L min^{-1} was pulled through the cavity. These flow conditions resulted in an operating pressure inside the cavity of ~ 470–500 torr. This sub-ambient cavity pressure had to be actively addressed due to the sensitivity of optical cavities to fluctuations in pressure (which can de-align the mirrors). This was accomplished by the addition of stabilizing mounts for the mirrors to prevent movement during measurements. Figure 4 contains a plumbing diagram for the CE-DOAS system with arrows indicating the direction of air flow at various points along the sampling line. Two pumps and three Mass Flow Controllers (MFCs) were used in this system, the main flow through the sampling line was set at ~ 120 L min^{-1} (controlled by MFC 1), the smaller sample flow through the cavity was set at ~ 9 L min^{-1} (controlled by MFC 2), and the calibration gases for the Fast-LED-CE-DOAS system (used for monitoring cavity performance and determining cavity path length) were controlled by MFC 3. Photographs of the inlet, operational cavity, and instrument rack containing all controlling electronics and spectrometer can be found in the Supplement Fig. S1.

AMTD
7, 6245–6285, 2014

3 Results

3.1 Instrument characterization

The following sections will describe the characterization of instrument properties pertinent to the measurement of fluxes via the EC technique.

3.1.1 Phase correction (N_2 pulse)

Wind sensor data was collected at 10 Hz and in order to calculate the glyoxal fluxes the CE-DOAS measurements needed to be synchronized to this data. Rather than degrading the high resolution wind data, the CE-DOAS measurements were first interpolated from 2 Hz to 10 Hz. Since the trace gas is drawn through an inlet, there is a finite time difference between the instantaneous wind velocity measurements and those of the trace gas measurements. The flux system deployed here includes a method for experimentally determining this correction. The method is described in detail in Bariteau et al. (2010), so only a brief overview will be given here: the inlet is equipped with a fast-switching solenoid valve that injects pure nitrogen (supplied from a compressed air cylinder) into the sample flow. The valve is triggered for 3–5 s at the beginning of every hour and the signal used as the trigger is recorded on the same timestamp as the anemometer. This data is used in conjunction with the accompanied drop in the trace gas signal (recorded on a different timestamp) to continuously monitor, and apply a correction to the time stamps prior to correlating both sensors. In the cavity, the measurement of O_4 was used for this correction. Figure 5 contains a plot showing an example of the corrected O_4 signal overlaid on the nitrogen pulse signal (black trace), also shown is the fit of the step response function from method 1 (blue trace, see below). The raw O_4 measurements are shown as black circles, and the interpolated data are the smaller red circles. Two methods were used to determine the phase correction based on the drop in the O_4 signal: (1) fitting of a first order step response function; (2) manual determination. Method 2 involved using O_4 data averages to identify when

AMTD
7, 6245–6285, 2014

the N_2 was attenuating the O_4 signal, and from there determining the time at which the signal actually started dropping. Each analysis was performed on hourly data files; 626 files were analyzed and 50 of these files did not meet basic criteria to enable the pulse matching and so were rejected; the total number of usable hours for the flux data was 576. The average difference found between the two phase correction methods was 0.11 s and the statistics associated with each analysis can be found in Table 2.

3.1.2 Response time

The pulse of nitrogen described in the previous section was also used to characterize the response time of the instrument. Introducing pure N_2 gas into the sample flow created a drop in the O_4 signal which was exploited to determine the response time of the instrument. The same two methods employed for the phase correction were used to calculate the instrument response time, which also gave an average difference between methods of 0.11 s (statistics in Table 2). The instrument response is best determined experimentally, since high frequency flux attenuations can be caused by drawing the sample through the aerosol filter and long sampling line. Here, a low-pass filter function was chosen to represent the attenuation.

$$H(f) = \frac{1}{1 + (2\pi f \tau_c)^2} \tag{3}$$

where τ_c is the instrument response time.

Using the measured response time and the filter function, the instrument cut-off frequency (f_c) (the frequency at which the signal fluctuations drop by $1/\sqrt{2}$) was calculated, which corresponds to a drop in the signal to 0.5.

$$f_c = \frac{1}{2\pi\tau_c} \tag{4}$$

Using the average values of the response time of 0.283 s and 0.282 s for the first-order step response function and the manual determination, respectively, the calculated cut-off frequency is 0.56 Hz. The application of the filter function for this system and the

AMTD
7, 6245–6285, 2014

effect of the response time on the high frequency attenuation will be discussed in Sect. 3.3.1. These small differences in response time determined from the two methods add certainty about the correction of the flux measurements, as is discussed in more detail in Sect. 3.3.3.

3.1.3 Fast measurements

The variance spectra for glyoxal as a function of frequency for a 6 h time period on 4 February 2012 from 15:00–21:00 UTC are shown in Fig. 6. Data from both 10 min (purple) and 30 min (light blue) averaging periods (see Sect. 3.3.2) are included in this plot.

The constant variance per Hz in the frequency range sampled by the instrument demonstrates that the Fast-LED-CE-DOAS system is indeed a white noise sensor. The horizontal black line represents the integral of the data in the frequency range 6×10^{-4} to 1 Hz of $\sim 1585\,\mathrm{pptv}^2$. The solid vertical black line depicts the cut-off frequency of the instrument calculated from the average response time of the instrument, and the dashed vertical black lines represent ± 1 standard deviation of this data.

3.2 Diurnal cycle measurements

Analyzing data created from summing 1000 spectra ($\sim$ 8 min total integration time) enabled the measurement of a diurnal cycle of glyoxal between 2–28 February 2012. A time series of these measurements can be found in Fig. 7 (top panel, left axis). Summing 1000 spectra allowed the realization of an average RMS value of $(1.0 \pm 0.1) \times 10^{-4}$, which translates into an average detection limit of 5.9 pptv; lower detection limits are possible from further averaging of the data. Included in Fig. 7 are time traces for in situ O_3, solar zenith angle (SZA), NO_2, RH, ambient air temperature, ambient pressure, wind speed (from the sonic anemometer), and a flag indicating periods that were suitable for EC fluxes.

AMTD
7, 6245–6285, 2014

3.3 Ambient flux measurements

3.3.1 Signal attenuation

As introduced in Sect. 3.1.2, a low-pass filter function was used to assess the high frequency flux attenuation due to the aerosol filter and sampling line length; Eq. (1) can be re-written as Eq. (5):

$$F_c = \overline{w'c'_{\mathrm{m}}} = \int_0^{f_{\mathrm{n}}} C_{\mathrm{wc}}(f)[H(f)]^{\frac{1}{2}}\mathrm{d}f = \int_0^{f_{\mathrm{n}}} C_{\mathrm{wcm}}(f)\mathrm{d}f \tag{5}$$

where the subscript m represents the measured values, see Eq. (1) for other variables (note that the square root appears in the modified equation because only the signal of the trace gas is attenuated).

This relationship can then be used to assess the effect of attenuation on the overall flux by applying the filter function using the Kaimal model neutral-stability cospectrum (Kaimal et al., 1972), derived via Eqs. (6a) and (6b)

$$\frac{fC_{\mathrm{wc}(f)}}{F_{\mathrm{c}}} = \frac{11n}{(1+13.3n)^{1.75}}, \quad n \leq 1.0 \tag{6a}$$

$$\frac{fC_{\mathrm{wc}(f)}}{F_{\mathrm{c}}} = \frac{11n}{(1+3.8n)^{2.4}}, \quad n \geq 1.0 \tag{6b}$$

where the surface normalized frequency $n = fz/\overline{u_{\mathrm{r}}}$, z is the measurement height, and $\overline{u_{\mathrm{r}}}$ is the average relative wind speed. Using the calculated "true" and "measured"

AMTD
7, 6245–6285, 2014

Kaimail cospectra, an attenuation ratio (R_{attn}) was derived.

$$R_{\mathrm{attn}}(z,\overline{u_{\mathrm{r}}}) = \frac{\int_0^{f_{\mathrm{n}}} C_{\mathrm{wc\_K}}(f,z,\overline{u_{\mathrm{r}}})[H(f)]^{\frac{1}{2}}\mathrm{d}f}{\int_0^{f_{\mathrm{n}}} C_{\mathrm{wc\_K}}(f,z,\overline{u_{\mathrm{r}}})\mathrm{d}f} = \frac{\int_0^{f_{\mathrm{n}}} C_{\mathrm{wcm\_K}}(f,z,\overline{u_{\mathrm{r}}})\mathrm{d}f}{\int_0^{f_{\mathrm{n}}} C_{\mathrm{wc\_K}}(f,z,\overline{u_{\mathrm{r}}})\mathrm{d}f} = \frac{\int_0^{f_{\mathrm{n}}} C_{\mathrm{wcm}}(f,z,\overline{u_{\mathrm{r}}})\mathrm{d}f}{\int_0^{f_{\mathrm{n}}} C_{\mathrm{wc}}(f,z,\overline{u_{\mathrm{r}}})\mathrm{d}f} = \frac{F_{x\mathrm{m}}}{F_x} \tag{7}$$

where $C_{\mathrm{wc\_K}}$ denotes the Kaimal cospectrum. For the calculation of this ratio, the average value of 0.282 s for the instrument response time was used in the filter response function $H(f)$. The assessment of this data leads to an average attenuation ratio of 0.947, but never resulted in more than a 10 % correction.

3.3.2 Flux filtering and results

Two different averaging periods for the glyoxal and vertical wind velocity data were used to determine the glyoxal flux: 10 min and 30 min, each segment containing a 50 % overlap with following segments (11 segments per hour for 10 min data, and 3 segments per hour for 30 min data). Both averaging periods were used for the data derived from the two methods used for determining the phase correction, creating a total of 4 different flux data sets. Basic filtering criteria were applied to the averaged data segments to reject measurements from undesirable wind sectors (± 60° relative wind direction and less than 10° standard deviation) and excessive ship maneuvers (maximum 25° heading range). Additional filtering criteria were applied to exclude outliers in the flux data through the assessment of the horizontal components of the glyoxal flux and the rate of change of glyoxal for each data segment. These filter values were chosen rather arbitrarily through a visual inspection of the data. No significant differences were found between the 4 data sets. Only results from the 30 min data determined from phase correction method 2 will be discussed. While individual flux measurements

AMTD
7, 6245–6285, 2014

proved to be noisy, further binning of the 30 min flux measurements reveals trends in the data. Figure 8 contains example cospectra from this data, where the average of all data (green trace) scatters around zero. The examples of both positive (red trace) and negative (blue trace) cospectra were created by binning data: from 16 February 21:15–17 February 00:45 LT (positive cospectrum); and from 2 February 14:45–15:45 LT (negative cospectrum).

3.3.3 Error sources

The potential sources of error in this data are: (1) inaccuracies in determining the phase shift of the CE-DOAS measurements; (2) high frequency signal loss due to sampling line attenuation; and (3) uncertainty surrounding the noisy raw glyoxal measurements. Phase shift determination was deemed to be rather robust (through the comparison of the values determined using the two different methods), and any small inaccuracies would have negligible effect on the flux data (as assessed by comparing the results from the 4 methods previously mentioned). The high frequency flux loss due to signal attenuation was calculated as being, at most, 10 % from the characterization in the instrument response time. Based on the cospectra (Fig. 8), it seems that glyoxal efficiently transferred through the sample lines and using the O_4 measurements to characterize sample transfer gives reasonably good agreement.

4 Discussion and conclusions

The Fast-LED-CE-DOAS instrument is a multispectral sensor suitable to measure eddy covariance (EC) fluxes of glyoxal in the remote marine boundary layer (MBL). The measurement frequency of ~ 2 Hz is sufficient to capture ~ 90 % of the glyoxal flux. Inlet and sampling line attenuation was determined using the measured response time of the instrument (0.28 ± 0.14 s, based on O_4 measurements) and accounts for a correction of < 10 %. Multiple gases are selectively detected simultaneously with glyoxal, and are

AMTD
7, 6245–6285, 2014

exploited for our flux measurements as follows: NO_2 measurements are used to identify and filter data affected by stack contamination from the ship; H_2O measurements are used to measure ambient relative humidity; O_4 measurements are used an internal calibration gas to assure control over cavity alignment and mirror cleanliness (Thalman and Volkamer, 2010); further the pulsing of nitrogen gas into the inlet is monitored from fast high signal-to-noise measurements of O_4 as part of individual spectra. O_4 is then used to characterize sample transfer time through the sampling line, and to synchronize the clocks of the chemical sensor with that of the wind sensor. Two different methods showed excellent control over the phase correction from O_4 measurements (average difference $\sim 0.11 \pm 0.10$ s), and give confidence in the EC flux measurements of glyoxal.

We have performed the first in situ measurements of glyoxal volume mixing ratios (VMRs) over oceans, and present first EC flux measurements of this soluble and short-lived molecule. Data from the first field deployment of the instrument is presented (26 days of measurements). For the VMR data a persistent diurnal trend is observed: glyoxal mixing ratios peak just before dawn (1 h average maximum in the NH: 43 ± 2 pptv; minimum: 26 ± 1 pptv; maximum SH: 61 ± 1 pptv; minimum: 39 ± 2 pptv), decrease during the day, and reach a minimum in the late evening just after dark (1 h average maximum in the NH: 36 ± 1 pptv; minimum: 16 ± 1 pptv; maximum SH: 48 ± 2 pptv; minimum: 24 ± 1 pptv); followed by continuous increase through the night. The day-to-day variability in glyoxal is significantly larger than the accuracy of our instrument. Major advantages with the Fast LED-CE-DOAS instrument to perform precise and accurate measurements of glyoxal are its inherent calibration from observing O_4 (see above) as well as direct calibration from knowledge of the absorption cross section of glyoxal (Volkamer et al., 2005). An earlier prototype version of our instrument has undergone detailed comparison with a large variety of state-of-the-art glyoxal measurement techniques (Thalman et al., 2014). In short, these comparisons revealed an excellent performance compared to other measurement techniques and virtually negligible systematic bias over a wide variety of laboratory conditions. LED-CE-DOAS measurements were

AMTD
7, 6245–6285, 2014

found to have the lowest limit of detection (LOD), showed the lowest amount of scatter during calibration experiments (highly precise), and are deemed accurate to within 1–2 pptv glyoxal, or 3.5 % at high signal-to-noise, whichever is higher. This uncertainty is smaller than the typical multiday variability in glyoxal over oceans. Indeed, the error bars for multiday averaged data reflect this variability (standard deviation), rather than the instrument precision/accuracy. Despite this significant day-to-day variability, some trends can be seen if data is segregated as a function of time of day (local time) and geographical location. Figure 9 shows the VMR (panel a) and EC flux data (panel b) binned as a function of time of day. The data were further segregated for measurements collected in the Northern Hemisphere (NH, blue, 13° N to 0°) and Southern Hemisphere (SH, red, 0° to 10° S); the global average of all data is shown as the grey trace. The number of data points within each bin is given in Table 3. For the flux data the error bars reflect the 90 % confidence intervals of data within each bin. The shaded regions in the background indicate daytime (yellow) and nighttime (grey), and the average SZA (minimum indicates solar noon) is further shown for reference on the right axis.

The campaign averaged VMR (all data) was 36 ± 9 pptv glyoxal. This is slightly less glyoxal compared to first measurements of glyoxal inside the MBL that found ∼ 80 pptv over the Sargasso Sea (Zhou and Mopper 1990). It is possible that some continental outflow of terrestrial glyoxal might have contributed to these elevated glyoxal VMR. (Sinreich et al., 2010) reported ∼ 63 ± 21 pptv daytime glyoxal over the remote Eastern tropical Pacific Ocean, which is in marginal agreement with the campaign average VMR of our in situ measurements. Recent reports of an average ∼ 25 pptv glyoxal, and no more than 40 pptv, over a wide array of ocean environments (Majajan et al., 2014) are slightly lower than our in situ observations. The comprehensive evidence generally supports the global presence of glyoxal over oceans as indicated by satellites (Wittrock et al., 2006; Lerot et al., 2010). Global glyoxal observations currently remain unexplained by atmospheric models (Myriofekalitakis et al., 2008; Fu et al., 2008; Stavrakou et al., 2009), and retrievals remain uncertain (Lerot et al., 2010), and largely untested.

AMTD
7, 6245–6285, 2014

Global measurements of glyoxal from satellites agree that the Eastern Pacific Ocean is a global hotspot for glyoxal over oceans (Wittrock et al., 2006; Lerot et al., 2010). In this context it is interesting to note that measurements by Sinreich et al. (2010) in a similar season and in a region that borders that probed here towards the East found average concentration of 63 ± 21 pptv that agree only marginally within error bounds with the in situ measurements presented in this study. This raises questions about a longitudinal variation in glyoxal at tropical latitudes, which had been observed by some satellites (Wittrock et al., 2006), but not by others (Lerot et al., 2010). Our in situ measurements in the NH probe a reasonably large longitude range and help assess this question. We do not find any obvious variation of glyoxal as a function of longitude. The average glyoxal VMR in the westerly NH cruise segment is 32 ± 5 pptv (average over 7 days; 13° N to 0° latitude; 133° W to 105° W longitude), compared to 31 ± 8 pptv in the easterly NH cruise segment (average over 7 days; 13° N to 0° latitude; 105° W to 80° W longitude). Early reports from SCIAMACHY found the annually averaged (year 2005) vertical column density (VCD) of 4.5×10^{14} and 6.0×10^{14} molec cm^{-2} VCD over the western and eastern cruise segments in the NH; and 3.5×10^{14} molec cm^{-2} over the SH cruise segment (Wittrock et al., 2006). Interestingly, measurements from the Global Ozone Monitoring Experiment-2 (GOME-2) satellite (Lerot et al., 2010) report $\sim 4.5 \times 10^{14}$ molec cm^{-2} in both regions of the NH, i.e., find no evidence for a longitudinal variation in multi-year averaged data (2007 to 2009); and $\sim 3 \times 10^{14}$ molec cm^{-2} over the SH cruise segment. The absence of a gradient over 3000 km distance in GOME-2 data is consistent with our data. However, it is interesting to note that the lower limit VCDs of both satellite instruments correspond to ~ 183 pptv glyoxal in the NH, and ~ 120 pptv glyoxal in the SH (assuming all glyoxal is located inside a 1 km high MBL). Such high glyoxal is not confirmed by our observations, or by the measurements of Sinreich et al. (2010). We note that the maximum concentration of 140 pptv reported by Sinreich et al. (2010) presents an extremely rare scenario that is not deemed representative of this dataset (see their Fig. 3c). In situ and ship MAX-DOAS column observations (Sinreich et al., 2010; Mahajan et al., 2014) agree that there is insufficient

AMTD
7, 6245–6285, 2014

glyoxal inside the MBL to explain satellite VCDs; this is particularly true over the NH tropical Eastern Pacific Ocean (by a factor 2 to 6). Furthermore, our in situ data show glyoxal is more abundant in the SH tropical MBL. By contrast, both satellites find ~ 25–42 % lower glyoxal VCDs in the SH compared to the NH. The campaign average VMR during mornings in the SH (47 ± 7 pptv glyoxal) corresponds to ~ 1.2×10^{14} molec cm^{-2} glyoxal VCD over the SH cruise segment, which is 2–3 times lower than long-time average VCD observed from space. The reason for this apparent mismatch in glyoxal amounts, and reversed hemispheric gradient is currently not understood. A particularly interesting development to investigate the diurnal variation of glyoxal over oceans consists in the Tropospheric Emissions: Monitoring of Pollution (TEMPO) satellite mission (planned to launch in 2019), which will provide first time-resolved glyoxal VCD observations from geostationary orbit. Our diurnal profiles show further that glyoxal concentrations change by 30 % over the course of the day. With the caveat that changes in MBL VMRs may not be indicative of VCD changes, this also implies that ~ 15 % lower VCDs are expected at the time of the OMI satellite overpass (13:45 LT at equator). The differences between satellite and in situ measurements are as of yet difficult to reconcile. Notably, a direct comparison between in situ observations and column data is complicated due to the lack of vertical profile measurements of glyoxal at tropical latitudes, different averaging times, and spatial scales probed by in situ and column observations, as well as uncertain assumptions about a priori profiles, cloud screening, and other factors that influence air mass factor calculations. Some of these factors were further investigated from collocated measurements of glyoxal from aircraft during the TORERO project. The fast in situ LED-CE-DOAS instrument holds great potential for future deployments on research aircraft.

The diurnal variations in our glyoxal flux measurements qualitatively reflect the variations in the VMRs seen in Fig. 9. The maximum fluxes are seen at night (SH: $(5.3 \pm 3.3) \times 10^{-2}$ pptv m s^{-1}; NH: $(2.3 \pm 3.1) \times 10^{-2}$ pptv m s^{-1}) and minimum fluxes during the daytime (SH: $(-1.6 \pm 3.8) \times 10^{-2}$ pptv m s^{-1}; NH: $(-5.6 \pm 4.1) \times 10^{-2}$ pptv m s^{-1}). All nighttime fluxes in the SH are significantly greater

AMTD
7, 6245–6285, 2014

than zero (SH nighttime average: $(4.7 \pm 1.8) \times 10^{-2}$ pptv m s^{-1}). By contrast the daytime fluxes are significantly negative (NH daytime average: $(-4.6 \pm 2.3) \times 10^{-2}$ pptv m s^{-1}). Assuming a dry deposition velocity of 1×10^{-3} m s^{-1} and using an average day time mixing ratio of glyoxal in the NH of 30 pptv results in an estimated flux towards the ocean of 3×10^{-2} pptv m s^{-1}, which is within the error of the measurements. Furthermore, the source of glyoxal from the ocean to the atmosphere is surprising, since glyoxal is so water soluble. Previous observations of positive fluxes of less soluble OVOCs, such as acetaldehyde, have been attributed to super-saturation of subsurface waters in acetaldehyde (Zhou and Mopper, 1990; Yang et al., 2014). Glyoxal formation in subsurface waters cannot explain a positive flux to the atmosphere. This is because of the very large effective Henry's Law coefficient ($K_H = 4.2 \times 10^5$ M atm^{-1}), which causes the equilibrium of glyoxal to be strongly shifted ($10^7 : 1$) towards the ocean (Volkamer et al., 2009). The high K_H value of glyoxal is the result of rapid hydration reactions; once hydrated, glyoxal exists primarily in mono- and di-hydrated forms (Ruiz-Montoya and Rodriguez-Mellado 1994, 1995) that give rise to the 3–5 orders of magnitude higher K_H value of glyoxal compared to other OVOC (see Table 1). Ervens and Volkamer (2010) estimated the hydration rate of glyoxal to be 7 s^{-1}. This corresponds to a lifetime of glyoxal with respect to hydrolysis of ~ 140 ms. Unless glyoxal escapes from the ocean within this time-frame, it will hydrate and is trapped in hydrated forms in the condensed phase. Using Eq. (8)

$$D = \frac{l^2}{2t} \tag{8}$$

where D is the diffusion coefficient (assuming a range $(0.001–1) \times 10^{-5}$ cm^2 s^{-1}, Finlayson-Pitts and Pitts, 2000), l is distance, and t is time, we estimate that the time scale of hydration of glyoxal corresponds to a diffusive length scale of only ~ 0.5–17 µm. Such a short distance rules out glyoxal production in sub-surface waters as a source for the positive glyoxal flux. The observation of the positive glyoxal fluxes at night thus locates a glyoxal source inside the organic sea surface microlayer (SML).

AMTD
7, 6245–6285, 2014

The maximum average positive (net) flux that we observe in the SH at night (5.3×10^{-2} pptv m s^{-1}) corresponds to a primary glyoxal accumulation in a 500 m high MBL of about ~ 4 pptv over a period of 12 h. This corresponds to ~ 30 % of the increase in the VMR of glyoxal that is actually being observed over the course of the night. We note that the EC technique measures a net flux, i.e., only the difference between deposition and emission fluxes contributes to the observed chemical gradients that we correlate with vertical gradients in winds. Based on the variability in the net-flux, it appears that both processes are contributing to the signal. Given the high solubility of glyoxal, the fraction of the glyoxal molecules which deposit to the surface and are later re-emitted is likely small. Thus, we assume that the deposition is essentially a 100 % efficient sink and the emission we see is due to instantaneous production/emission on the surface monolayer. The actual surface production rate is hence the sum of deposition and the observed net-flux. However, even assuming extreme values for the deposition flux the maximum possible surface production flux is ~ 10×10^{-2} pptv m s^{-1}, and accounts for ~ 60 % of the glyoxal VMR increase over night. It appears that an additional source of glyoxal is operational in addition to that in the SML that is not captured by the EC flux method. Moreover, the observed daytime negative flux of glyoxal indicates some unknown gas phase source of glyoxal, and likely other OVOCs in the MBL. While negative or neutral fluxes have also been observed for acetone and methanol (Marandino et al., 2005; Yang et al., 2013, 2014), both of these molecules live sufficiently long (acetone: 15 days; methanol: 13 days) that transport from terrestrial sources is likely to contribute to their abundance in the remote MBL. By contrast, any glyoxal lost to the ocean has been produced locally. The daytime lifetime of glyoxal (~ 2 h) is too short to explain this source in terms of transport from terrestrial sources.

The widespread positive flux that we observe in both hemispheres at night (more prevalent in the SH) provides direct evidence that the SML is widespread (Wurl et al., 2011), and that oxidation reactions inside the SML are a source for OVOCs. Notably, a recent laboratory study observed the volatilization of several OVOCs (including glyoxal) when O_3 was flowed above a polyunsaturated fatty acid film on artificial saltwater

AMTD
7, 6245–6285, 2014

in a flow reactor (Zhou et al., 2014). These results provide qualitative confirmation that the oxidation of the SML by O_3 can be a source for OVOCs to the gas-phase. However, the production rates found in this laboratory study are insufficient to explain any appreciable portion of the observed glyoxal over the tropical Pacific Ocean. The sources of glyoxal in the remote MBL deserve further investigation.

The Supplement related to this article is available online at doi:10.5194/amtd-7-6245-2014-supplement.

Acknowledgements. The development of the Fast LED-CE-DOAS sensor was supported by the US National Science Foundation under NSF-CAREER award (ATM-847793). The TORERO project is a US-SOLAS contribution, and supported by NSF under award (AGS-I104104, PI: R. Volkamer). S. Coburn is recipient of a NASA Earth and Space Science Fellowship. The authors thank the captain and crew of the RV *Ka'imimoana* during the "TORERO cruise" KA-12-01, as well as Brian Lake, David Welsh, and the NOAA TAO program for their great support.

References

Baldocchi, D., Falge, E., Gu, L., Olson, R., Hollinger, D., Running, S., Anthoni, P., Bernhofer, C., Davis, K., Evans, R., Fuentes, J., Goldstein, A., Katul, G., Law, B., Lee, X., Malhi, Y., Meyers, T., Munger, W., Oechel, W., U, K., Pilegaard, K., Schmid, H., Valentini, R., Verma, S., Vesala, T., Wilson, K., and Wofsy, S.: FLUXNET: a new tool to study the temporal and spatial variability of ecosystem-scale carbon dioxide, water vapor, and energy flux densities, B. Am. Meteorol. Soc., 82, 2415–2434, doi:10.1175/1520-0477(2001)082<2415:FANTTS>2.3.CO;2, 2001.

Bariteau, L., Helmig, D., Fairall, C. W., Hare, J. E., Hueber, J., and Lang, E. K.: Determination of oceanic ozone deposition by ship-borne eddy covariance flux measurements, Atmos. Meas. Tech., 3, 441–455, doi:10.5194/amt-3-441-2010, 2010.

Bell, T. G., De Bruyn, W., Miller, S. D., Ward, B., Christensen, K. H., and Saltzman, E. S.: Air–sea dimethylsulfide (DMS) gas transfer in the North Atlantic: evidence for limited interfacial

gas exchange at high wind speed, Atmos. Chem. Phys., 13, 11073–11087, doi:10.5194/acp-13-11073-2013, 2013.

Blomquist, B. W., Fairall, C. W., Huebert, B. J., Kieber, D. J., and Westby, G. R.: DMS sea-air transfer velocity: direct measurements by eddy covariance and parameterization based on the NOAA/COARE gas transfer model, Geophys. Res. Lett., 33, L07601, doi:10.1029/2006GL025735, 2006.

Blomquist, B. W., Huebert, B. J., Fairall, C. W., and Faloona, I. C.: Determining the sea-air flux of dimethylsulfide by eddy correlation using mass spectrometry, Atmos. Meas. Tech., 3, 1–20, doi:10.5194/amt-3-1-2010, 2010.

Blomquist, B. W., Fairall, C. W., Huebert, B. J., and Wilson, S. T.: Direct measurement of the oceanic carbon monoxide flux by eddy correlation, Atmos. Meas. Tech., 5, 3069–3075, doi:10.5194/amt-5-3069-2012, 2012.

Blomquist, B. W., Huebert, B. J., Fairall, C. W., Bariteau, L., Edson, J. B., Hare, J. E., and McGillis, W. R.: Advances in air–sea CO_2 flux measurement by Eddy correlation, submitted, 2014.

Coburn, S., Dix, B., Sinreich, R., and Volkamer, R.: The CU ground MAX-DOAS instrument: characterization of RMS noise limitations and first measurements near Pensacola, FL of BrO, IO, and CHOCHO, Atmos. Meas. Tech., 4, 2421–2439, doi:10.5194/amt-4-2421-2011, 2011.

Edson, J. B., Hinton, A. A., Prada, K. E., Hare, J. E., and Fairall, C. W.: Direct covariance flux estimates from mobile platforms at sea, J. Atmos. Ocean. Techn., 15, 547–562, doi:10.1175/1520-0426(1998)015<0547:DCFEFM>2.0.CO;2, 1998.

Edson, J. B., Fairall, C. W., Bariteau, L., Zappa, C. J., Cifuentes-Lorenzen, A., McGillis, W. R., Pezoa, S., Hare, J. E., and Helmig, D.: Direct covariance measurement of CO_2 gas transfer velocity during the 2008 Southern Ocean Gas Exchange Experiment: wind speed dependency, J. Geophys. Res.-Oceans, 116, C00F10, doi:10.1029/2011JC007022, 2011.

Ervens, B. and Volkamer, R.: Glyoxal processing by aerosol multiphase chemistry: towards a kinetic modeling framework of secondary organic aerosol formation in aqueous particles, Atmos. Chem. Phys., 10, 8219–8244, doi:10.5194/acp-10-8219-2010, 2010.

Fairall, C. W., White, A. B., Edson, J. B., and Hare, J. E.: Integrated shipboard measurements of the marine boundary layer, J. Atmos. Ocean. Tech., 14, 338–359, doi:10.1175/1520-0426(1997)014<0338:ISMOTM>2.0.CO;2, 1997.

AMTD
7, 6245–6285, 2014

Fairall, C. W., Hare, J. E., Edson, J. B., and McGillis, W. R.: Parameterization and micrometeorological measurement of air–sea gas transfer, Bound.-Lay. Metorol., 96, 63–106, doi:10.1023/A:1002662826020, 2000.
Finlayson-Pitts, B. and Pitts, J. N.: Chemistry of the Upper and Lower Atmosphere: Theory, Experiments, and Applications, Academic Press, USA, 2000.
Fu, T., Jacob, D. J., Wittrock, F., Burrows, J. P., Vrekoussis, M., and Henze, D. K.: Global budgets of atmospheric glyoxal and methylglyoxal, and implications for formation of secondary organic aerosols, J. Geophys. Res.-Atmos., 113, D15303, doi:10.1029/2007JD009505, 2008.
Grosjean, D., Grosjean, E., and Gertler, A. W.: On-road emissions of carbonyls from light-duty and heavy-duty vehicles, Environ. Sci. Technol., 35, 45–53, doi:10.1021/es001326a, 2001.
Hays, M. D., Geron, C. D., Linna, K. J., and Smith, N. D.: Speciation of gas-phase and fine particle emissions from burning of foliar fuels, Environ. Sci. Technol., 36, 2281, doi:10.1021/es0111683, 2002.
Helmig, D., Lang, E. K., Bariteau, L., Boylan, P., Fairall, C. W., Ganzeveld, L., Hare, J. E., Hueber, J., and Pallandt, M.: Atmosphere-ocean ozone fluxes during the TexAQS 2006, STRATUS 2006, GOMECC 2007, GasEx 2008, and AMMA 2008 cruises, J. Geophys. Res.-Atmos., 117, D04305, doi:10.1029/2011JD015955, 2012.
Huebert, B., Blomquist, B., Hare, J., Fairall, C., Johnson, J., and Bates, T.: Measurement of the sea-air DMS flux and transfer velocity using eddy correlation, Geophys. Res. Lett., 31, L23113, doi:10.1029/2004GL021567, 2004.
Kaimal, J., Izumi, Y., Wyngaard, J., and Cote, R.: Spectral characteristics of surface-layer turbulence, Q. J. Roy. Meteorol. Soc., 98, 563–589, doi:10.1002/qj.49709841707, 1972.
Kean, A. J., Grosjean, E., and Grosjean, D.: On-road measurement of carbonyls in California light-duty vehicle emissions, Environ. Sci. Technol., 35, 4198–4204, doi:10.1021/es010814v, 2001.
Kieber, R., Zhou, X., and Mopper, K.: Formation of carbonyl-compounds from UV-induced photodegradation of humic substances in natural waters: fate of riverine carbon in the sea, Limnol. Oceanogr., 35, 1503–1515, 1990.
Kondo, F. and Tsukamoto, O.: Air-sea CO_2 flux by eddy covariance technique in the equatorial Indian Ocean, J. Oceanogr., 63, 449–456, doi:10.1007/s10872-007-0040-7, 2007.
Lenschow, D. and Raupach, M.: The attenuation of fluctuations in scalar concentrations through sampling tubes, J. Geophys. Res.-Atmos., 96, 15259–15268, doi:10.1029/91JD01437, 1991.

AMTD
7, 6245–6285, 2014

Lerot, C., Stavrakou, T., De Smedt, I., Müller, J.-F., and Van Roozendael, M.: Glyoxal vertical columns from GOME-2 backscattered light measurements and comparisons with a global model, Atmos. Chem. Phys., 10, 12059–12072, doi:10.5194/acp-10-12059-2010, 2010.

Liggio, J., Li, S., and McLaren, R.: Reactive uptake of glyoxal by particulate matter, J. Geophys. Res.-Atmos., 110, D10304, doi:10.1029/2004JD005113, 2005.

Mahajan, A. S., Prados-Roman, C., Hay, T. D., Lampel, J., Pöhler, D., Großmann, K., Tschritter, J., Frieß, U., Platt, U., Johnston, P., Kreher, K., Wittrock, F., Burrows, J. P., Plane, J. M. C., and Saiz-Lopez, A.: Glyoxal observations in the global marine boundary layer, J. Geophys. Res.-Atmos., 119, 6160–6169, doi:10.1002/2013JD021388, 2014.

Marandino, C. A., De Bruyn, W. J., Miller, S. D., Prather, M. J., and Saltzman, E. S.: Oceanic uptake and the global atmospheric acetone budget, Geophys. Res. Lett., 32, L15806, doi:10.1029/2005GL023285, 2005.

Marandino, C. A., De Bruyn, W. J., Miller, S. D., and Saltzman, E. S.: Eddy correlation measurements of the air/sea flux of dimethylsulfide over the North Pacific Ocean, J. Geophys. Res.-Atmos., 112, D03301, doi:10.1029/2006JD007293, 2007.

Marandino, C. A., De Bruyn, W. J., Miller, S. D., and Saltzman, E. S.: DMS air/sea flux and gas transfer coefficients from the North Atlantic summertime coccolithophore bloom, Geophys. Res. Lett., 35, L23812, doi:10.1029/2008GL036370, 2008.

Marandino, C. A., De Bruyn, W. J., Miller, S. D., and Saltzman, E. S.: Open ocean DMS air/sea fluxes over the eastern South Pacific Ocean, Atmos. Chem. Phys., 9, 345–356, doi:10.5194/acp-9-345-2009, 2009.

McGillis, W., Edson, J., Hare, J., and Fairall, C.: Direct covariance air-sea CO_2 fluxes, J. Geophys. Res.-Oceans, 106, 16729–16745, doi:10.1029/2000JC000506, 2001.

McGillis, W., Edson, J., Zappa, C., Ware, J., McKenna, S., Terray, E., Hare, J., Fairall, C., Drennan, W., Donelan, M., DeGrandpre, M., Wanninkhof, R., and Feely, R.: Air-sea CO_2 exchange in the equatorial Pacific, J. Geophys. Res.-Oceans, 109, C08S02, doi:10.1029/2003JC002256, 2004.

Miller, S., Marandino, C., de Bruyn, W., and Saltzman, E. S.: Air-sea gas exchange of CO_2 and DMS in the North Atlantic by eddy covariance, Geophys. Res. Lett., 36, L15816, doi:10.1029/2009GL038907, 2009.

Miller, S. D., Marandino, C., and Saltzman, E. S.: Ship-based measurement of air-sea CO_2 exchange by eddy covariance, J. Geophys. Res.-Atmos., 115, D02304, doi:10.1029/2009JD012193, 2010.

AMTD
7, 6245–6285, 2014

Millet, D. B., Guenther, A., Siegel, D. A., Nelson, N. B., Singh, H. B., de Gouw, J. A., Warneke, C., Williams, J., Eerdekens, G., Sinha, V., Karl, T., Flocke, F., Apel, E., Riemer, D. D., Palmer, P. I., and Barkley, M.: Global atmospheric budget of acetaldehyde: 3-D model analysis and constraints from in-situ and satellite observations, Atmos. Chem. Phys., 10, 3405–3425, doi:10.5194/acp-10-3405-2010, 2010.

Myriokefalitakis, S., Vrekoussis, M., Tsigaridis, K., Wittrock, F., Richter, A., Brühl, C., Volkamer, R., Burrows, J. P., and Kanakidou, M.: The influence of natural and anthropogenic secondary sources on the glyoxal global distribution, Atmos. Chem. Phys., 8, 4965–4981, doi:10.5194/acp-8-4965-2008, 2008.

Norman, M., Rutgersson, A., Sorensen, L. L., and Sahlee, E.: Methods for estimating air–sea fluxes of CO_2 using high-frequency measurements, Bound.-Lay. Meteorol., 144, 379–400, doi:10.1007/s10546-012-9730-9, 2012.

Platt, U.: Differential Optical Absorption Spectroscopy (DOAS), in: Air Monitoring by Spectroscopic Techniques, edited by: Sigrist, M. W., John Wiley & Sons, Inc., New York, 127, 1994.

Platt, U., Perner, D., and Patz, H.: Simultaneous measurement of atmospheric CH_2O, O_3, and NO_2 by differential optical-absorption, J. Geophys. Res.-Oceans, 84, 6329–6335, doi:10.1029/JC084iC10p06329, 1979.

Ruiz-Montoya, M. and Rodriguez-Mellado, J. M.: Use of convolutive potential sweep voltammetry in the calculation of hydration equilibrium constants of α-dicarbonyl compounds, J. Electroanal. Chem., 370, 183–187, 1994.

Ruiz-Montoya, M. and Rodriguez-Mellado, J. M.: Hydration constants of carbonyl and dicarbonyl compounds comparison between electrochemcial and no electrochemcial techniques, Portugaliae Electrochim. Acta, 13, 299–303, 1995.

Ryerson, T. B., Andrews, A. E., Angevine, W. M., Bates, T. S., Brock, C. A., Cairns, B., Cohen, R. C., Cooper, O. R., de Gouw, J. A., Fehsenfeld, F. C., Ferrare, R. A., Fischer, M. L., Flagan, R. C., Goldstein, A. H., Hair, J. W., Hardesty, R. M., Hostetler, C. A., Jimenez, J. L., Langford, A. O., McCauley, E., McKeen, S. A., Molina, L. T., Nenes, A., Oltmans, S. J., Parrish, D. D., Pederson, J. R., Pierce, R. B., Prather, K., Quinn, P. K., Seinfeld, J. H., Senff, C. J., Sorooshian, A., Stutz, J., Surratt, J. D., Trainer, M., Volkamer, R., Williams, E. J., and Wofsy, S. C.: The 2010 California Research at the Nexus of Air Quality and Climate Change (CalNex) field study, J. Geophys. Res.-Atmos., 118, 5830–5866, doi:10.1002/jgrd.50331, 2013.

Sinreich, R., Coburn, S., Dix, B., and Volkamer, R.: Ship-based detection of glyoxal over the remote tropical Pacific Ocean, Atmos. Chem. Phys., 10, 11359–11371, doi:10.5194/acp-10-11359-2010, 2010.

Stavrakou, T., Müller, J.-F., De Smedt, I., Van Roozendael, M., Kanakidou, M., Vrekoussis, M., Wittrock, F., Richter, A., and Burrows, J. P.: The continental source of glyoxal estimated by the synergistic use of spaceborne measurements and inverse modelling, Atmos. Chem. Phys., 9, 8431–8446, doi:10.5194/acp-9-8431-2009, 2009.

Taddei, S., Toscano, P., Gioli, B., Matese, A., Miglietta, F., Vaccari, F. P., Zaldei, A., Custer, T., and Williams, J.: Carbon dioxide and acetone air–sea fluxes over the southern Atlantic, Environ. Sci. Technol., 43, 5218–5222, doi:10.1021/es8032617, 2009.

Thalman, R. and Volkamer, R.: Inherent calibration of a blue LED-CE-DOAS instrument to measure iodine oxide, glyoxal, methyl glyoxal, nitrogen dioxide, water vapour and aerosol extinction in open cavity mode, Atmos. Meas. Tech., 3, 1797–1814, doi:10.5194/amt-3-1797-2010, 2010.

Thalman, R. and Volkamer, R.: Temperature dependent absorption cross-sections of O_2–O_2 collision pairs between 340 and 630 nm and at atmospherically relevant pressure, Phys. Chem. Chem. Phys., 15, 15371–15381, doi:10.1039/c3cp50968k, 2013.

Thalman, R., Baeza-Romero, M. T., Ball, S. M., Borrás, E., Daniels, M., Goodall, I., Henry, S. B., Karl, T., Keutsch, F., Saewung, K., Mak, J., Monks, P., Muñoz, A., Orlando, J., Peppe, S., Rickard, A., Ródenas, M., Pilar, S., Seco, R., Su, S., Tyndall, G., Vásquez, M., Vera, T., Waxman, E., and Volkamer, R.: Instrument inter-comparison of glyoxal, methyl glyoxal and NO_2 under simulated atmospheric conditions, Atmos. Meas. Tech. Discuss., in preparation, 2014.

van Pinxteren, M. and Herrmann, H.: Glyoxal and methylglyoxal in Atlantic seawater and marine aerosol particles: method development and first application during the Polarstern cruise ANT XXVII/4, Atmos. Chem. Phys., 13, 11791–11802, doi:10.5194/acp-13-11791-2013, 2013.

Vandaele, A. C., Hermans, C., Simon, P. C., Carleer, M., Colin, R., Fally, S., Mérienne, M. F., Jenouvrier, A., and Coquart, B.: Measurements of the NO_2 absorption cross-section from 42 000 cm^{-1} to 10 000 cm^{-1} (238–1000 nm) at 220 K and 294 K, J. Quant. Spectrosc. Ra., 59, 171–184, doi:10.1016/S0022-4073(97)00168-4, 1998.

Volkamer, R., Spietz, P., Burrows, J., and Platt, U.: High-resolution absorption cross-section of glyoxal in the UV-vis and IR spectral ranges, J. Photoch. Photobio. A, 172, 35–46, doi:10.1016/j.jphotochem.2004.11.011, 2005.

AMTD
7, 6245–6285, 2014

Volkamer, R., San Martini, F., Molina, L. T., Salcedo, D., Jimenez, J. L., and Molina, M. J.: A missing sink for gas-phase glyoxal in Mexico City: formation of secondary organic aerosol, Geophys. Res. Lett., 34, L19807, doi:10.1029/2007GL030752, 2007.

Volkamer, R., Ziemann, P. J., and Molina, M. J.: Secondary Organic Aerosol Formation from Acetylene (C_2H_2): seed effect on SOA yields due to organic photochemistry in the aerosol aqueous phase, Atmos. Chem. Phys., 9, 1907–1928, doi:10.5194/acp-9-1907-2009, 2009.

Vrekoussis, M., Wittrock, F., Richter, A., and Burrows, J. P.: Temporal and spatial variability of glyoxal as observed from space, Atmos. Chem. Phys., 9, 4485–4504, doi:10.5194/acp-9-4485-2009, 2009.

Waxman, E. M., Dzepina, K., Ervens, B., Lee-Taylor, J., Aumont, B., Jimenez, J. L., Madronich, S., and Volkamer, R.: Secondary organic aerosol formation from semi- and intermediate-volatility organic compounds and glyoxal: relevance of O/C as a tracer for aqueous multiphase chemistry, Geophys. Res. Lett., 40, 978–982, doi:10.1002/grl.50203, 2013.

Wittrock, F., Richter, A., Oetjen, H., Burrows, J. P., Kanakidou, M., Myriokefalitakis, S., Volkamer, R., Beirle, S., Platt, U., and Wagner, T.: Simultaneous global observations of glyoxal and formaldehyde from space, Geophys. Res. Lett., 33, L16804, doi:10.1029/2006GL026310, 2006.

Wurl, O., Wurl, E., Miller, L., Johnson, K., and Vagle, S.: Formation and global distribution of sea-surface microlayers, Biogeosciences, 8, 121–135, doi:10.5194/bg-8-121-2011, 2011.

Yang, M., Nightingale, P. D., Beale, R., Liss, P. S., Blomquist, B., and Fairall, C.: Atmospheric deposition of methanol over the Atlantic Ocean, P. Natl. Acad. Sci. USA, 110, 20034–20039, doi:10.1073/pnas.1317840110, 2013.

Yang, M., Beale, R., Liss, P., Johnson, M., Blomquist, B., and Nightingale, P.: Air–sea fluxes of oxygenated volatile organic compounds across the Atlantic Ocean, Atmos. Chem. Phys. Discuss., 14, 8015–8061, doi:10.5194/acpd-14-8015-2014, 2014.

Zhou, S., Gonzalez, L., Leithead, A., Finewax, Z., Thalman, R., Vlasenko, A., Vagle, S., Miller, L.A., Li, S.-M., Bureekul, S., Furutani, H., Uematsu, M., Volkamer, R., and Abbatt, J.: Formation of gas-phase carbonyls from heterogeneous oxidation of polyunsaturated fatty acids at the air–water interface and of the sea surface microlayer, Atmos. Chem. Phys., 14, 1371–1384, doi:10.5194/acp-14-1371-2014, 2014.

Zhou, X. and Mopper, K.: Apparent partition-coefficients of 15 carbonyl-compounds between air and seawater and between air and fresh-water – implications for air sea exchange, Environ. Sci. Technol., 24, 1864–1869, doi:10.1021/es00082a013, 1990.

AMTD
7, 6245–6285, 2014

Table 1. Overview of Eddy Covariance flux measurements from ships.

Molecule	MBL Concentration (pptv)	K_H ($M\,atm^{-1}$)	Lifetime* (days)	Reference flux measurement in MBL
CO_2	380–400 ($\times 10^6$)	0.035	$> 3 \times 10^5$	Fairall et al. (2000)
CO	60–150 ($\times 10^3$)	1×10^{-3}	16	Blomquist et al. (2012)
Acetone	700–900	30.3	10	Yang et al. (2014)
O_3	10–30 ($\times 10^3$)	0.011	6	Bariteau et al. (2010)
Methanol	300–900	222	4	Marandino et al. (2005)
DMS	20–1500	0.485	0.8	Hubert et al. (2004)
Acetaldehyde	200–300	14.1	0.2	Yang et al. (2014)
Glyoxal	25–80	4.2×10^5	9×10^{-2}	This work

* Lifetimes calculated against reaction with OH (assuming $[OH] = 3 \times 10^6$ molec cm^{-3}), and photolysis rates calculated for aerosol free, noon time at equator conditions.

AMTD
7, 6245–6285, 2014

Table 2. The average phase correction and time response of the Fast-LED-CE-DOAS instrument (with standard deviation) for the two different methods employed in this study. See text for details.

	Method 1		Method 2	
	Phase Correction (s)	Time Response (s)	Phase Correction (s)	Time Response (s)
Average	−2.54	0.28	−2.61	0.28
Standard Deviation	0.23	0.16	0.24	0.14

AMTD
7, 6245–6285, 2014

Table 3. Number of points in each time bin from Fig. 9.

Time Range	VMR Data All Data	VMR Data Northern Hemisphere	VMR Data Southern Hemisphere	Flux Data All Data	Flux Data Northern Hemisphere	Flux Data Southern Hemisphere
00:00–04:00 LT	494 249	287 844	206 405	195	110	85
02:00–06:00 LT	501 180	302 666	198 514	193	108	85
04:00–08:00 LT	465 714	300 299	165 415	170	103	67
06:00–10:00 LT	400 277	286 933	113 344	137	95	42
08:00–12:00 LT	412 463	275 280	137 183	141	92	49
10:00–14:00 LT	457 785	288 476	169 309	149	92	57
12:00–16:00 LT	495 793	297 908	197 885	157	88	69
14:00–18:00 LT	473 626	262 280	211 346	162	85	77
16:00–20:00 LT	450 306	257 819	192 487	166	94	72
18:00–22:00 LT	486 072	290 658	195 414	183	108	75
20:00–00:00 LT	497 257	302 619	194 638	187	111	76

AMTD
7, 6245–6285, 2014

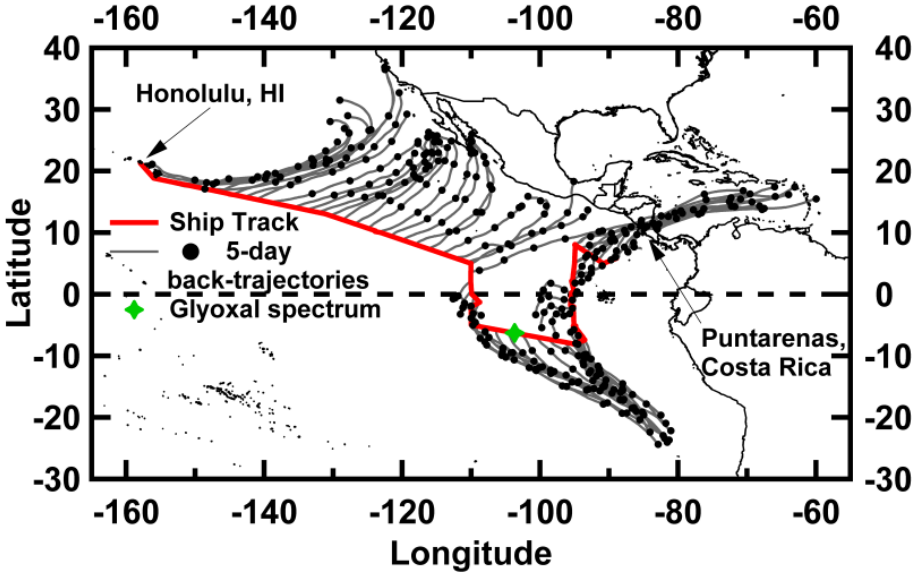

Figure 1. Cruise track of the NOAA RV *Ka'imimoana* during the TORERO 2012 field experiment (red trace). The ship set sail from Honolulu, HI on 25 January 2012 and made final port in Puntarenas, Costa Rica on 1 March 2012 (37 days at sea). Shown along the ship track are HYSPLIT 5-day back trajectories (initiated at 00:00 and 12:00 LT every day; solid grey lines). The black circles along the trajectories are spaced by 1 day. Air sampled in the Northern Hemisphere had been over the ocean for at least 2 days prior to reaching the ship, and often did not experience land influences for at least 5 days. Air sampled in the Southern Hemisphere had been over the ocean for more than 5 days without obvious land/pollution influences. The location of the example glyoxal spectrum is marked by the green star.

AMTD
7, 6245–6285, 2014

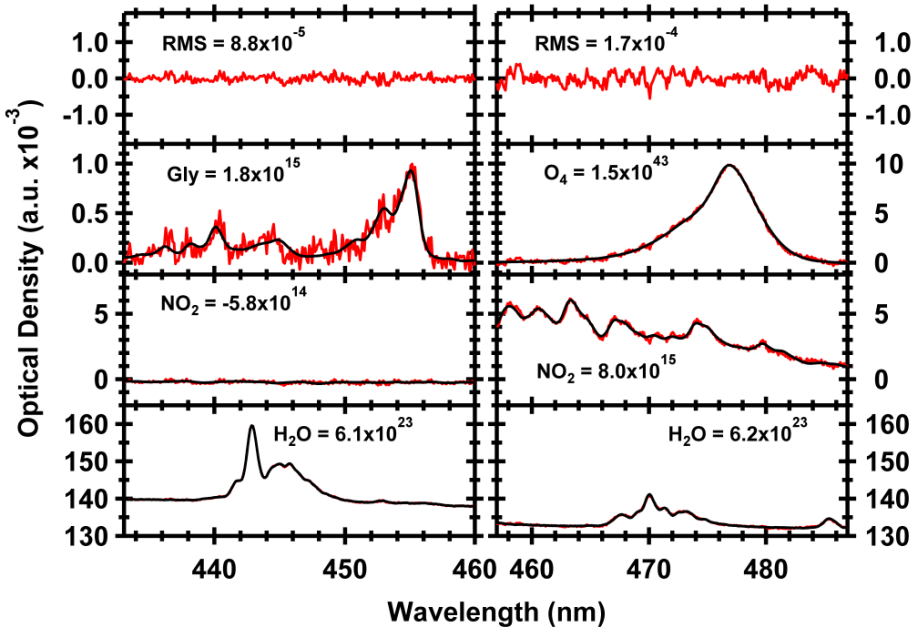

Figure 2. Example spectra of molecules measured by the Fast LED-CE-DOAS instrument. The DOAS fits are shown for glyoxal (left panel, 433–460 nm fit window), O_4 and NO_2 (right panel, 457–487 nm), and water vapor (both windows). The RMS residual for each fit is shown in the top row. The spectra shown here were recorded on 14 February 2012 at ~ 06:20 LT (glyoxal), and 11 February 2012 at ~ 13:40 LT (O_4).

AMTD
7, 6245–6285, 2014

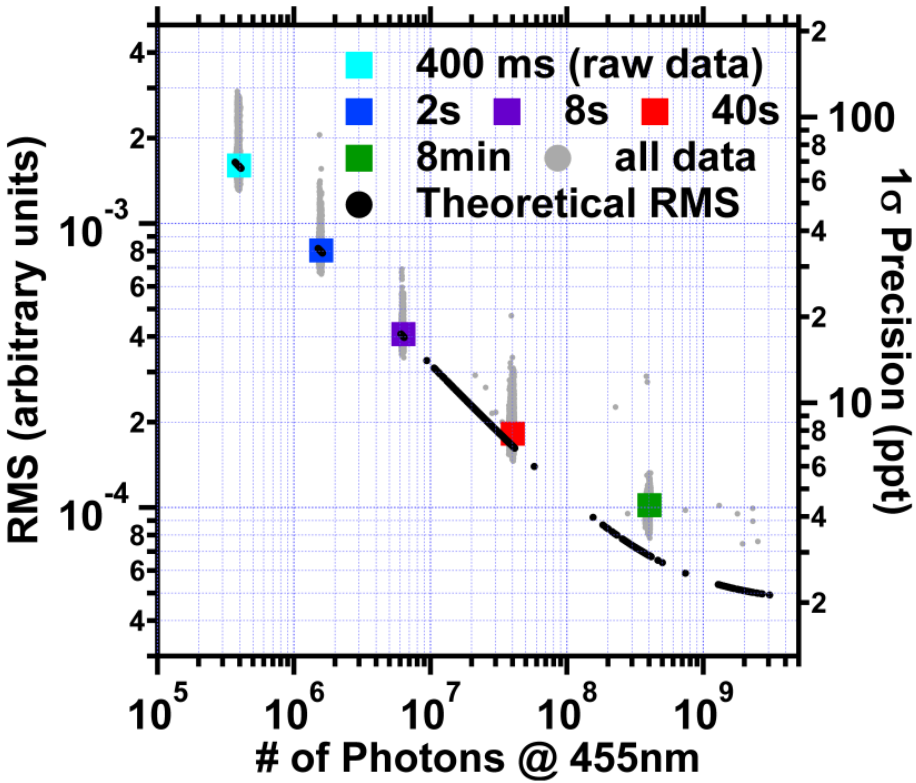

Figure 3. Fast LED-CE-DOAS instrument performance: sensitivity. The residual noise (RMS) from the DOAS analysis is shown as a function of the number of photons corresponding to different averaging of the data. Grey points represent all data, while colored squares represent their respective mean value; black circles represent the theoretical RMS value determined from photon counting statistics (Coburn et al., 2011). The corresponding 1σ precision of glyoxal is plotted on the right axis.

AMTD
7, 6245–6285, 2014

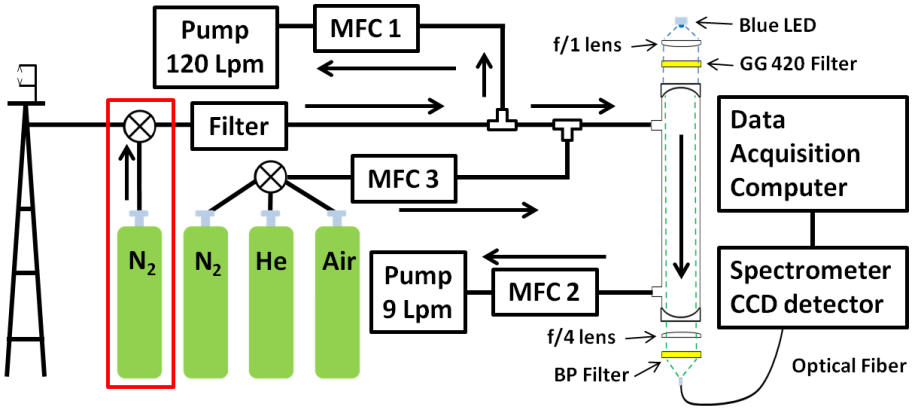

Figure 4. Sketch of the Fast-LED-CE-DOAS setup and plumbing diagram for sampling during TORERO 2012. The N_2 "puff" system is indicated by the red box. Arrows show the direction of flow through various portions of the system. Photographs of this set up can be found in Supplement Fig. S1.

AMTD
7, 6245–6285, 2014

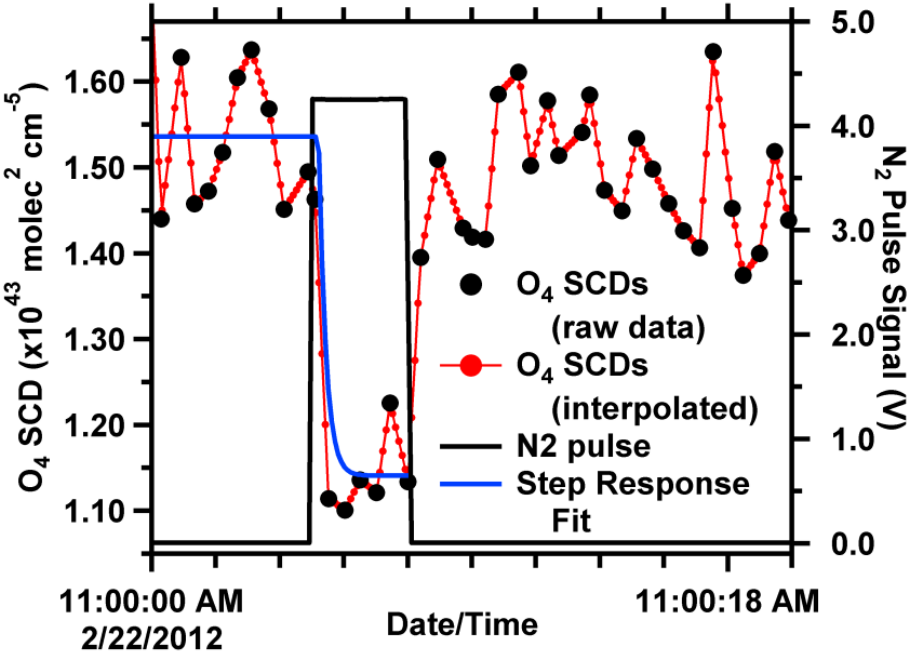

Figure 5. Illustration of the phase-correction and time response using O_4. Individual CE-DOAS O_4 measurements (black dots) were interpolated onto the timestamp of the wind sensor (red dots). The N_2 pulse signal (solid black line) is visible as the drop in O_4 SCDs; the data has already been time-shifted to match this N_2 trigger. Also shown is the fit of a step response function (solid blue line) to the drop in the O4 signal, from which an instrument time response can be determined.

AMTD
7, 6245–6285, 2014

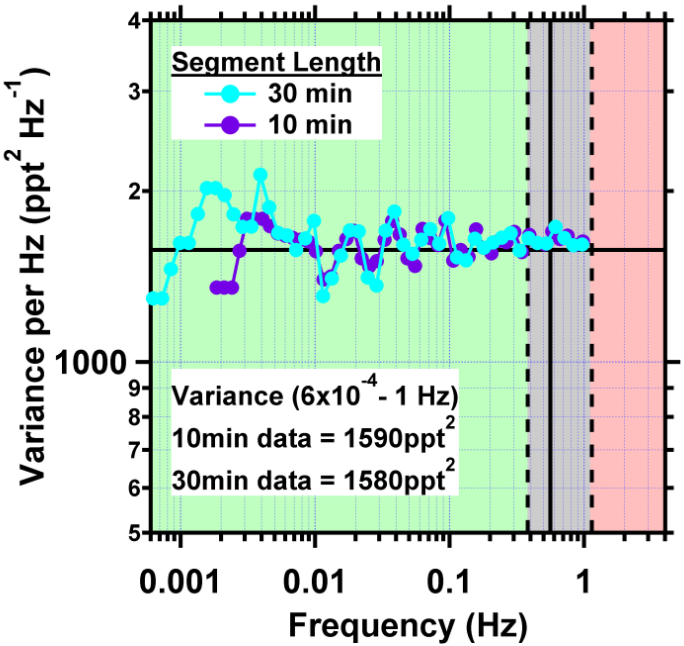

Figure 6. Fast LED-CE-DOAS instrument performance: frequency response for glyoxal. The glyoxal variance distribution per frequency bin is for a 1 h section of data (representative of the global average) on 22 February 2012 from 04:00–05:00 LT. The horizontal line represents the integral variance ($\sim 1600\,\mathrm{ppt}^2\,\mathrm{Hz}^{-1}$) at frequencies measured by the instrument (green shading). The solid vertical line represents the cut-off frequency determined from the average time response of the instrument; the dashed vertical lines represent the standard deviation of the time response data (grey background shading); higher frequencies were not measured by our setup (red shading). The Nyquist frequency of our setup is 1 Hz.

AMTD
7, 6245–6285, 2014

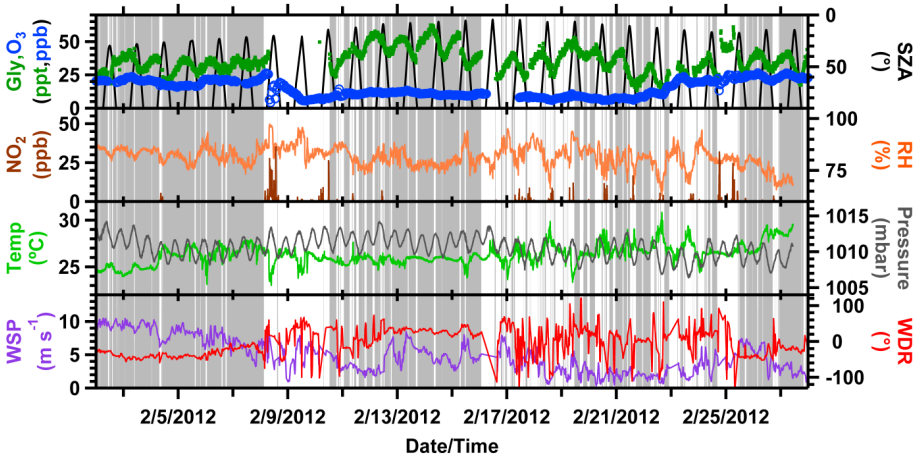

Figure 7. Time series of glyoxal, O_3 and NO_2, as well as meteorological parameters. Grey shaded background represents times suitable for flux calculations; filters included NO_2, cavity pressure, wind direction, wind direction standard deviation, ship heading range, $dGly/dt$, and the horizontal glyoxal flux components. See text and Supplement Fig. S2 for details.

AMTD
7, 6245–6285, 2014

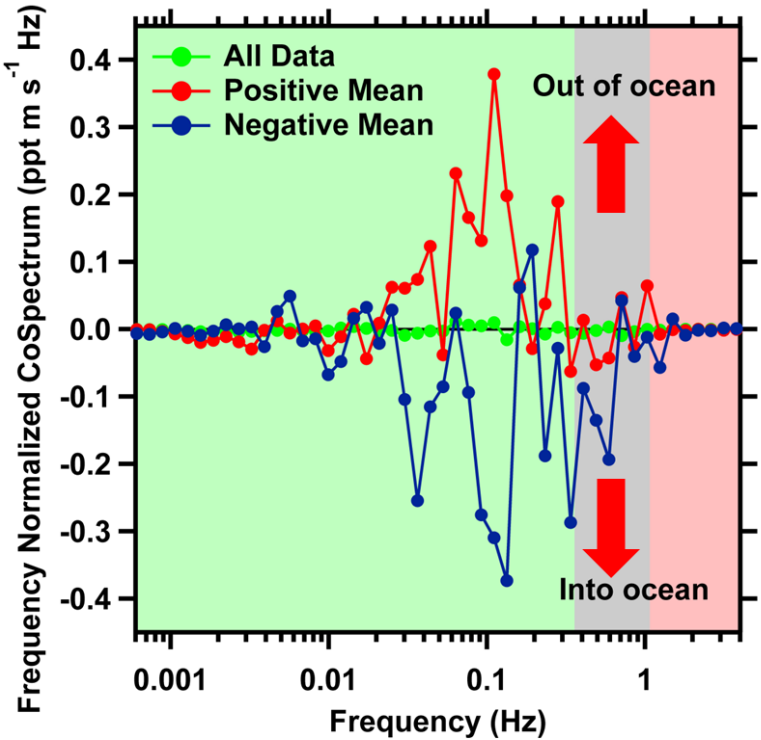

Figure 8. Cospectra of glyoxal and vertical wind from the flux calculations. The green trace represents the average of all cospectra that passed the quality assurance filters. The positive cospectrum (red) represents data averaged over a period of ~3.5 h from 16 February 2012 21:15 LT to 17 February 2012 00:45 LT. The negative cospectrum (blue) represents a ~1 h average on 2 February 2012 from 14:45–15:45 LT. The background color shading is identical to that in Fig. 6.

AMTD
7, 6245–6285, 2014

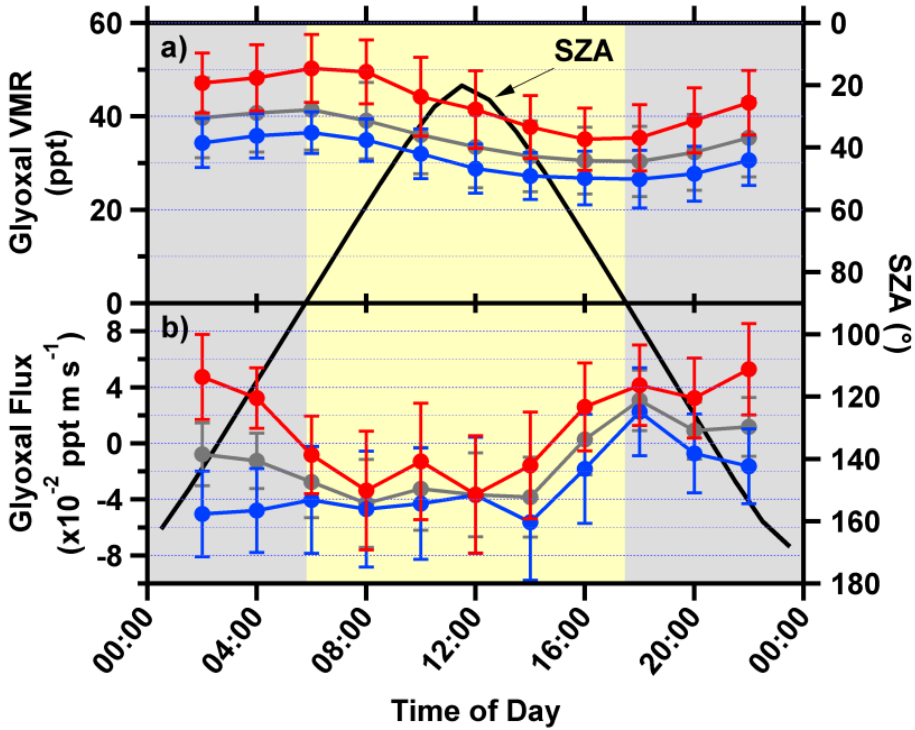

Figure 9. Diurnal variation in the glyoxal mixing ratio **(a)** and the glyoxal flux **(b)** in the Northern (blue) and Southern Hemisphere (red). Only data that qualifies for flux calculations has been averaged. Yellow shading indicates daytime, while grey indicates nighttime; the SZA is also shown on the right axis.

AMTD
7, 6245–6285, 2014